(Received 24 December 2024, Accepted 3 June 2025, Scheduled 22 August 2025)

A New Spatial Detection Technique Using New RF Codes for Microwave-Based Object Localization System

Mohd A. M. N. Azami[1], Mohamad Z. A. Abd Aziz[1, 2, *], Abd S. Ja'afar[1], Mohd R. Ahmad[1], Mohd F. Abd Malek[3], and Mohd S. Abu Talib[1]

[1] *Centre for Telecommunication Research and Innovation (CeTRI)*
Fakulti Teknologi dan Kejuruteraan Elektronik dan Komputer (FTKEK)
Universiti Teknikal Malaysia Melaka, Hang Tuah Jaya, Durian Tunggal, Melaka 76100, Malaysia
[2] *Centre of Technology for Disaster Risk Reduction (CDR)*
Fakulti Teknologi dan Kejuruteraan Elektronik dan Komputer (FTKEK)
Universiti Teknikal Malaysia Melaka, Hang Tuah Jaya, Durian Tunggal, Melaka 76100, Malaysia
[3] *Faculty of Engineering and Information Sciences, University of Wollongong in Dubai, United Arab Emirates*

ABSTRACT: Microwave-based object localization system is a noninvasive technique that uses microwave signals to detect, map, and analyze the properties of materials. This approach provides information about hidden objects within materials. However, the localization process can be complex, requiring sophisticated algorithms to interpret the signals accurately. This study proposes a new technique for microwave-based object localization system using Radio Frequency (RF) Codes to perform spatial detection with four pairs of RF Code sensors representing bits of "111", "110", "101", and "011". The system incorporates four identical RF Code paths arranged symmetrically around a circular container, improving spatial coverage and enabling accurate detection of hidden objects located at eight different spatial positions. Steel is used as the hidden object, while Stone serves as Material X in this system. The system achieved an average detection accuracy of 70% and a detection efficiency close to 100% across all spatial positions. Additionally, the RF Code performance chart is designed to interpret the detection accuracy results, making the analysis more accessible and practical. The proposed system has potential applications in nondestructive testing, material analysis, industrial inspection, and security systems, offering a reliable and efficient solution for detecting hidden or embedded objects.

1. INTRODUCTION

Microwave-based object localization system has gained significant attention as a noninvasive, high-resolution technique for detecting and analysing the internal structure of materials across a wide range of applications, including medical diagnostics, industrial nondestructive testing, and geophysical exploration [1–7]. Its ability to provide detailed information about the electromagnetic properties of materials, such as permittivity and conductivity, has made it particularly useful in scenarios where conventional imaging methods are ineffective. For instance, high-resolution millimeter-wave tomography, as discussed by Och et al. has been successfully employed for nondestructive testing of low-permittivity materials, offering a powerful tool for analysing structural integrity without physically altering the test object [8]. This method leverages spatial diversity and multi-view scanning techniques to reconstruct two-dimensional (2D) or three-dimensional (3D) images with exceptional clarity, making it a promising approach in both industrial and scientific contexts.

In the medical field, microwave-based object localization system has been extensively studied for its potential to revolutionize cancer detection, especially for breast cancer [9–12]. Benny et al. provide an overview of the advantages of microwave tomography in breast tumor detection, emphasizing its ability to provide a quantitative description of tissue permittivity, which helps differentiate between healthy and cancerous tissues [13]. Moreover, microwave-based object localization system offers a safer alternative to traditional methods like X-rays, as it avoids ionizing radiation, making it suitable for frequent monitoring. Recent advancements in this area have focused on improving the spatial resolution and reducing the complexity of reconstruction algorithms to ensure that microwave images can accurately depict even small tumors. AlSawaftah et al. highlight the potential of this technology for early breast cancer detection, where high-resolution images are critical for identifying malignancies at an early stage, offering a promising direction for future medical diagnostics [14].

Despite the growing adoption of microwave-based object localization system, several challenges persist, particularly in enhancing spatial resolution and refining image reconstruction processes. Advances in microwave near-field imaging have addressed some of these limitations by developing prototypes and systems capable of operating at higher frequencies and offering improved resolution [15]. The use of ultra-wideband microwave systems has further expanded the scope of microwave-based object localization system applications, allowing for better differentiation between materials with subtle permittivity

* Corresponding author: Mohamad Zoinol Abidin Abd Aziz (mohamadzoinol@utem.edu.my).

contrasts. Furthermore, deep learning techniques have been incorporated into microwave-based object localization system to overcome some of the traditional challenges in image [16, 17] reconstruction. Shao and Du explore the feasibility of using convolutional neural networks to enhance microwave-based object localization system accuracy, enabling the system to reconstruct images in a lower-dimensional space while maintaining essential features of the original structure. This approach significantly reduces the computational burden, making real-time imaging and analysis more achievable [18].

RF (Radio Frequency) Code is a code technique that uses RF as a code. The idea of RF Code comes from the reflection coefficients at different frequencies which are varied to encode data as shown in Fig. 1. This frequency-code technique allows a larger number of bits to be encoded on a relatively simple and low-cost sensor. One notable application of RF Code technology is in chipless Radio Frequency Identification (RFID) antenna tag design, where the absence of a microchip enables even simpler and more cost-effective implementations [19–29]. The unique reflection patterns across frequencies provide a reliable means of identifying and locating objects within the medium of detection.

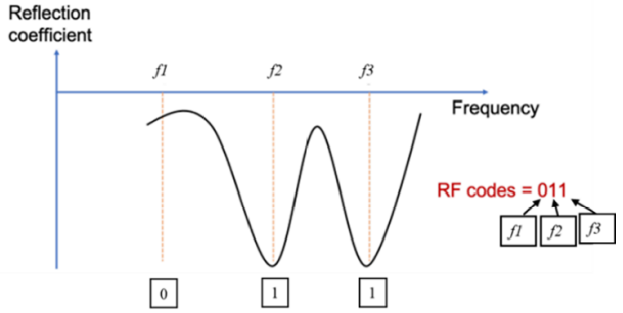

FIGURE 1. Frequency encode technique.

By employing multiple transmitting and receiving sensors that use specific codes, a system can exploit the spatial diversity offered by the antenna locations. This facilitates the application of compressed sensing techniques, enabling efficient reconstruction of the target's location and shape. Moreover, employing RF Codes can reduce system complexity and data processing requirements, resulting in faster imaging speeds and more efficient implementations. This study presents a novel method for a microwave-based object localization system using the RF Code technique to enhance spatial detection capability that:

1. Developed a spatial detection technique using multibit RF Code sensor configuration
2. Conducted detection experiments across eight positions
3. Introduced an intuitive RF Code Performance Chart

Unlike previous RF Code-based methods that primarily focused on object identification or tag encoding using chipless RFID approaches, the proposed technique introduces a new spatial detection mechanism by employing three-bit RF Code combinations (111, 110, 101, and 011), each representing a unique transmission path. These RF Code sensors are arranged in a circular layout, enabling signal propagation and detection from multiple directions. Instead of relying on image reconstruction or reflected signal analysis, the system analyzes the transmission loss to detect the presence of a hidden object. Detection decisions are made by comparing the measured signal difference (Y_{test}) against calculated thresholds (Y_{Max} and Y_{Min}), which allows for a low-complexity yet effective classification framework. This significantly reduces computational demand and enhances the system's suitability for real-time, low-cost applications. A comparison with previous methods has been provided in the revised manuscript to highlight the uniqueness and advantages of this work. Through detailed analysis and experimental validation, the detection accuracy has been presented, and this research highlights the potential advantages of the new technique across various applications.

2. THE MAIN SYSTEM

In this work, the proposed RF Code Microwave-Based Object Localization System detects and identifies hidden objects by transmitting and analysing microwave signals. The system consists of three main components: RF Code sensors, a Vector Network Analyzer (VNA), and a computer, as depicted in Fig. 2. RF Code sensors are strategically placed within the medium to transmit and receive microwave signals. These signals interact with the medium and any hidden objects before being sent to the VNA, which captures and evaluates the transmitted and reflected signal patterns. The measured data from the VNA is stored on a computer for further processing and analysis. Finally, an RF Code performance chart is generated based on the percentage of detection accuracy.

FIGURE 2. RF Code microwave-based object localization system.

2.1. RF Code Configuration

Four distinct RF Code sensors, identified by three bits which are bits "111", bits "110", bits "101", and bits "011", were designed, fabricated, and tested. These codes represent different sensor types, each tailored to operate at specific resonant frequencies within a multiband framework, ensuring minimal interference between frequencies. The resonant frequencies corresponding to each bit are as follows: for the first bit, 1.6 GHz ($\pm$0.1 GHz); for the second bit, 2.1 GHz ($\pm$0.1 GHz); and for the third bit, 2.6 GHz ($\pm$0.1 GHz).

A 0.5 GHz gap was strategically incorporated between resonant frequencies to minimize interference, enhancing the accuracy and reliability of the sensors. The simulation and optimization processes were conducted using Microwave Computer Simulation Technology (CST) Studio software, which allowed for precise adjustments to the sensor parameters before fabrication. After the design phase, the sensors were fabricated, and their performance was evaluated through return loss measurements. Return loss is a critical parameter indicating how well the sensor operates at its designated frequencies and was

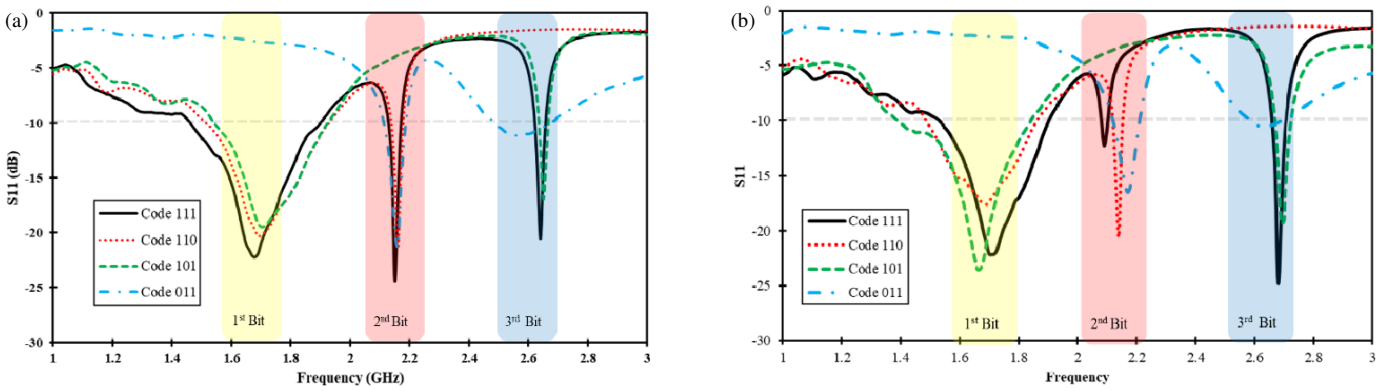

FIGURE 3. Result for (a) simulation and (b) measurement of S_{11} for all RF sensor codes, with showing of the resonant frequency for each bits.

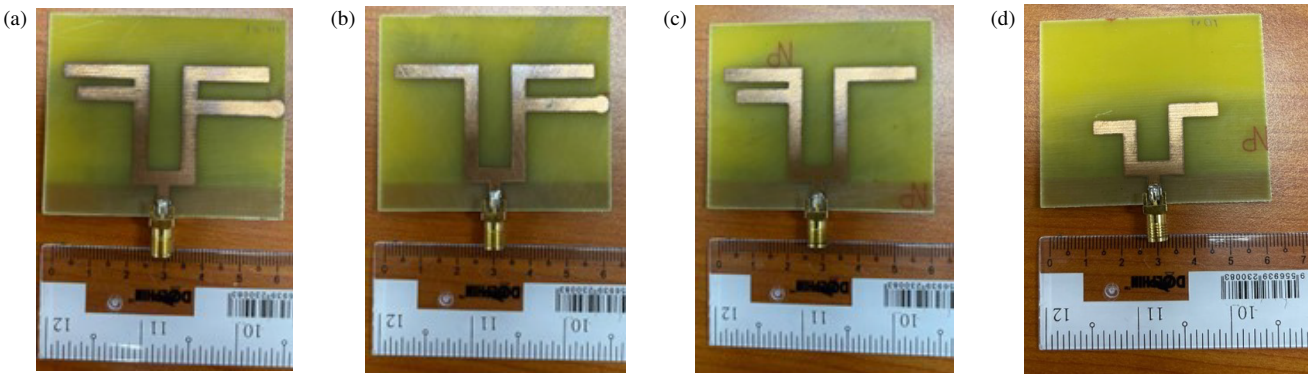

FIGURE 4. Picture of fabricated RF sensor of (a) Code 111, (b) Code 11, (c) Code 11 and (d) Code 011.

measured for each sensor Code 111 for bits 111, Code 110 for bits 110, Code 101 for bits 101, and until Code 011 for bits 011. The measured return loss values were compared with simulation results to validate the design. All sensors successfully achieved a minimum reflection coefficient of -10 dB, indicating efficient performance at the target frequencies. The measured resonant frequencies for each code closely aligned with the simulated values, confirming the accuracy of the design and fabrication processes.

The simulated and measured reflection coefficients for all codes are shown in Fig. 3. Table 1 shows the comparison between the resonant frequency and the return loss of both simulation and measurement for all codes. For Codes 111 and 110, the measured frequencies are slightly higher than the simulated frequency (e.g., $f1 = 1.67$ GHz vs 1.60 GHz for Code 111) and show greater return losses in dB, particularly in Code 111 where the measurement return losses at *f1* and *f2* (-22.49 dB, -24.54 dB) are better than the simulated frequency (-11.30 dB, -40.48 dB). Similarly, Codes 101 and 011 exhibit slight frequency shifts; however, the measured losses generally exceed the simulated result, especially for Code 011 at *f3* (-10.50 dB measured vs -12.21 dB simulated). Overall, while the simulation and measurement are aligned in trends, the observed shifts in frequency and increased measured losses suggest potential influences from material properties or experimental conditions. Fig. 4 shows the picture of all fabricated sensors.

TABLE 1. Comparison of S_{11} for simulation and measurement results.

Code		Simulation			Measurement		
		f1	*f2*	*f3*	*f1*	*f2*	*f3*
111	GHz	1.60	2.16	2.66	1.67	2.15	2.64
	dB	-11.30	-40.48	-14.21	-22.49	-24.54	-21.16
110	GHz	1.61	2.17	-	1.69	2.16	-
	dB	-11.75	-40.72	-	-20.28	-21.77	-
101	GHz	1.61	-	2.68	1.69	-	2.65
	dB	-12.00	-	-18.20	-22.03	-	-18.63
011	GHz	-	2.16	2.64	-	2.15	2.60
	dB	-	-30.19	-12.21	-	-20.55	-10.50

2.2. 4×4 Microwave-Based Object Localization System

After the fabrication process, the sensors for Codes 111, 110, 101, and 011 were used to develop the 4×4 Microwave-Based Object Localization System. Fig. 5 shows the illustration of setup of 4×4 Microwave-Based Object Localization System. The setup consists of transmitters and receivers, arranged symmetrically around a circular container. The sensors are placed such that they face each other, forming a circular pattern around the container. The distance between each transmitter and its corresponding receiver, across the diameter of the circle, is 20 cm. Each sensor is connected to a portable Vector Network Analyzer (NanoRFE V2 Plus4) which measures transmission

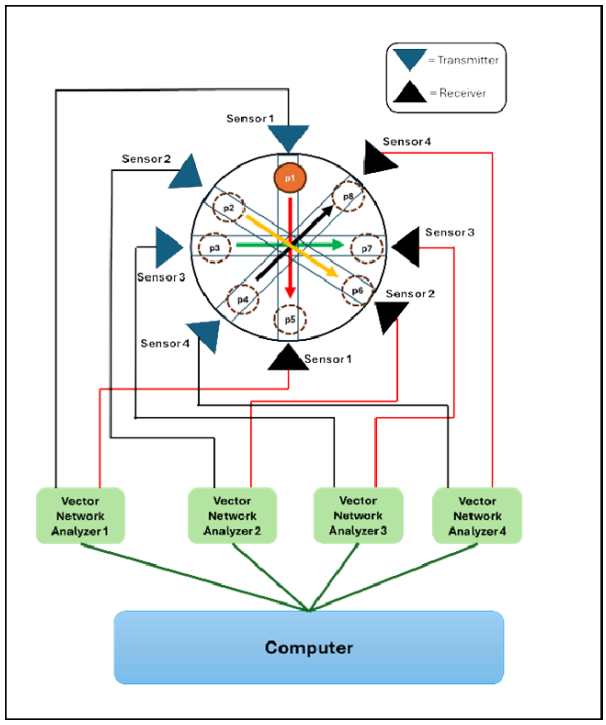

FIGURE 5. 4×4 microwave-based object localization system setup.

(S_{21}) and reflection (S_{11}) properties of the signals radiated between the sensors. Each pair of sensor codes defines a path corresponding to the transmission and reception of signals between a specific transmitter and receiver. The paths are named according to the codes assigned to the sensors, with each path representing the signal exchange between the corresponding code pairs. For example, the path for Code 111 referred to the transmission between the transmitter and receiver of Code 111, and for the other codes.

The circular container is positioned at the centre of the sensor array, placed on a stage elevated 20 cm above the table. This setup provides a controlled environment in which signals pass through the container and interact with the material inside. Each sensor is connected to a portable VNA to monitor and measure changes in signal transmission across the paths. The circular arrangement of sensors creates multiple intersecting signal paths, as shown in Fig. 5. This figure shows the 4×4 Microwave-Based Object Localization system setup for this experiment. The setup will be used for spatial detection measurements in the next stage.

3. ENVELOPE CORRELATION COEFFICIENT ANALYSIS

The correlation of the sensor arrangement can be calculated using Envelope Correlation Coefficient (ECC). ECC is used in Multiple-Input Multiple-Output (MIMO) systems to evaluate how independent the signals transmission path. It ranges from 0 to 1, with values close to 0 indicating low correlation (ideal for most communication systems) and values close to 1 indicating high correlation. In this work, ECC is used to identify the highest correlation for each proposed path. The goal for each proposed path is to achieve an ECC value close to 1.00, as it would indicate that the system is consistently detecting the change of the signal linearly. ECC can be calculated by using scattering parameters ECC equation shown in (1) [30].

$$\rho_e = \frac{\left|S_{11} * S_{12} + S_{21} * S_{22}\right|^2}{\left(1 - \left|S_{11}\right|^2 - \left|S_{21}\right|^2\right)\left(1 - \left|S_{22}\right|^2 - \left|S_{12}\right|^2\right)} \quad (1)$$

The selected setup of the configuration is shown in Fig. 6. The diagram represents a circular layout of transmitters and receivers, each labelled with a unique RF Code. The transmitters sensors are represented by blue triangles, and the receiver sensors are represented by black triangles. All sensors are positioned symmetrically around the circumference of a circle container. The transmitter sensors are placed on the left side of the circle, while the receiver sensors are positioned on the right side. The specific path codes are represented using arrows of different colours as shown in Fig. 6. For example, Path Code 101 is represented by a red arrow.

Table 2 shows the average of S-parameter measurements for 50 sets of data across various RF path codes at all frequencies. For example, the lowest S_{11} is -17.75 dB which is at *f1* for RF path Code 111, while the lowest S_{21} is -21.09 dB for *f3* at RF path Code 011. Table 3 presents the ECC values for each path code for all three frequencies. The lowest ECC value was observed at frequency *f1* across all RF path codes. At *f1*, RF path Code 110 recorded an ECC value of 0.87, while RF Code 111 had the lowest ECC value of 0.57. In contrast, at frequencies *f2* and *f3*, most sensors exhibited higher positive ECC values, approaching 1.00.

TABLE 2. The result of average S-parameter measurement.

RF Path Code	Freq	Average value of S-Parameter for 50 sets of measurement			
		S11 (db)	S21 (db)	S12 (db)	S22 (db)
111	*f1*	-17.75	-21.72	-21.71	-17.75
	f2	-12.66	-43.17	-43.16	-12.70
	f3	-8.15	-41.71	-41.71	-8.15
110	*f1*	-15.75	-23.70	-23.69	-15.70
	f2	-14.91	-33.74	-33.72	-14.92
101	*f1*	-10.78	-25.73	-25.71	-10.78
	f3	-7.50	-28.61	-28.60	-7.50
011	*f2*	-11.36	-24.17	-24.18	-11.36
	f3	-7.50	-21.09	-21.11	-7.50

4. SPATIAL DETECTION METHOD

The proposed sensor configuration in the previous section will be used in the next spatial detection measurement, and the setup

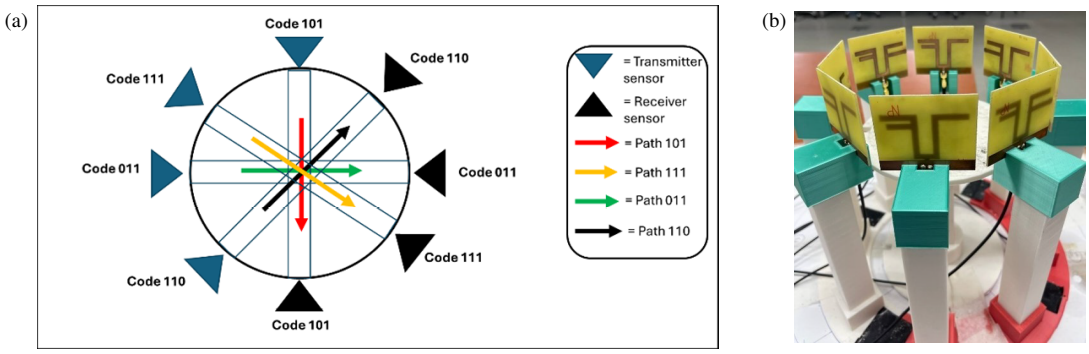

FIGURE 6. (a) RF Code sensors arrangements. (b) Actual measurement setup.

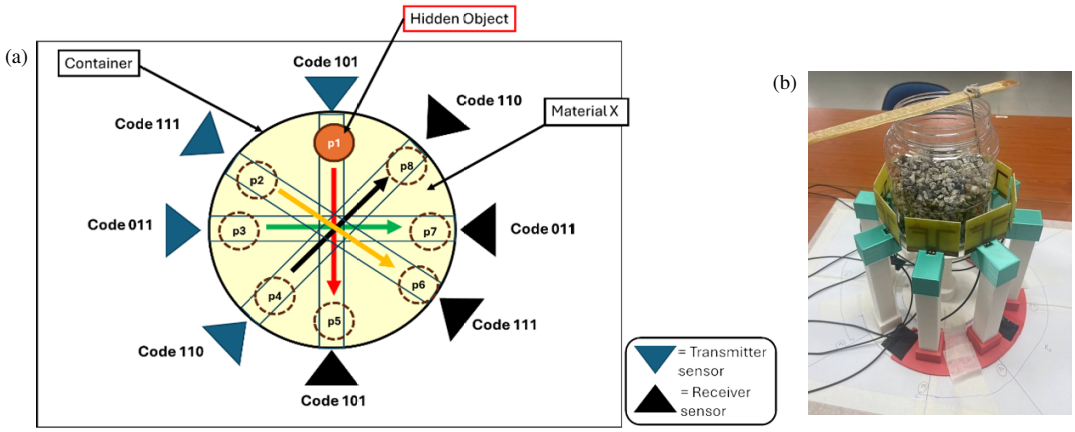

FIGURE 7. (a) Setup of spatial detection measurement. (b) Actual measurement setup.

TABLE 3. ECC value for all RF path codes.

RF path Code	Envelope Correlation Coefficient (ECC)		
	f1	*f2*	*f3*
111	0.57	0.98	1.00
110	0.87	0.92	
101	0.83		0.83
011		0.98	0.74

TABLE 4. Hidden object position for spatial detection at each RF path code.

RF path Code	Position of hidden object	
111	*p2*	*p6*
110	*p4*	*p8*
101	*p1*	*p5*
011	*p3*	*p7*

is shown in Fig. 7. It is called Spatial Detection Analysis. The steps in this analysis involved measuring the signal transmission path at each path code by analyzing S_{21} values and visualizing the result. In this experiment, a container holds the material used as the measurement medium, and this material refers to "Material X". A "hidden object" refers to any foreign material located inside Material X that requires detection. Fig. 7 and Fig. 5 show the setup in the Spatial Detection Analysis. In each path of code, there are two positions that have been decided to put the hidden object. One position is closer to the transmitter and the other position closer to the receiver. In total, there are eight positions for detecting the hidden object. The list of the positions is listed in Table 4.

The process begins by measuring the signal transmission across all path codes simultaneously, using the S_{21} parameter for Material X, referred to as x. The same process is then repeated with a hidden object placed inside Material X at path code *p1*, followed by *p5*. This arrangement corresponds to the RF path Code "101". The S_{21} result with the hidden object included is referred to as y. To determine the signal loss caused by the hidden object, the difference between y and x is calcu-

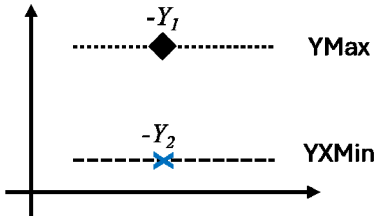

FIGURE 8. The S_{21} difference in Y in dB for range of detection.

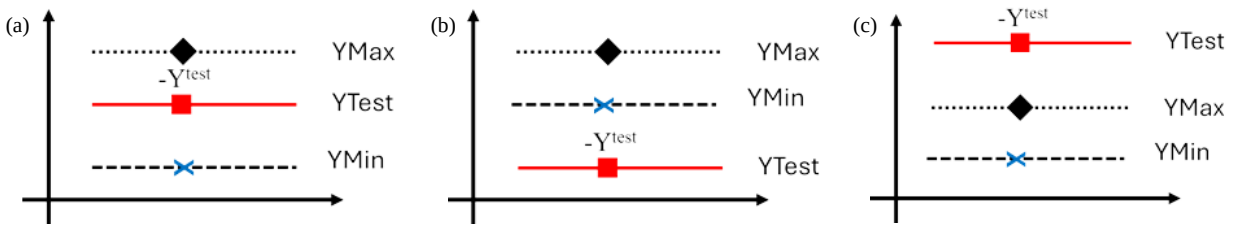

FIGURE 9. Graph of plotted Y_{test} with Y_{Max} and Y_{Min} with three cases, (a) Case 1, (b) Case 2 and (c) Case 3.

lated, denoted as Y ($Y = y - x$). This procedure is performed three times and repeated for all RF path codes.

After identifying the Y, it is assumed that $-Y_1$ is the maximum (Y_{Max}) and $-Y_2$ the minimum (Y_{Min}) difference among the three measurements. The plotted result of the difference is called Range of Detection, shown in Fig. 8 and Table 5. Fig. 8 will be used in identifying the classification at the next stage. This process measurement was done for all frequency codes (*f1*, *f2*, *f3*).

TABLE 5. Example of the difference between y and x.

	(y)	(x)	$(y-x)$
Measurement number	Value of y	Value of x	Difference (Y)
1	y_1	x_1	$-Y_1$
2	y_2	x_2	$-Y_2$
3	y_3	x_3	$-Y_3$

Let Y_{test} represent the measurement of S_{21} of hidden object position at specific path code. This process involves the measurement of new x_{test} and y_{test}, and three cases of Y_{test} values will be considered as shown in Fig. 9. The cases can be categorized as Case 1, if the value of Y_{test} is within Y_{Max} and Y_{Min}. Case 2 occurs when when the value of Y_{test} is lower than both Y_{Max} and Y_{Min} while Case 3 occurs when the value of Y_{test} is higher than both Y_{Max} and Y_{Min}. Fig. 9 shows the situation of each of the cases.

In Case 1, the plotted Y_{test} falls within the range of Y_{Max} and Y_{Min}. Meanwhile, for Case 2 and Case 3, Y_{test} is lower than Y_{Min} and higher than Y_{Max}, respectively. The detection accuracy for Case 1 and Case 2 is classified as 100% and 90%, respectively. Otherwise, for Case 3, the value of Y_{test} is larger than Y_{Max}. Cumulative Frequency Distribution (CFD) graph has been obtained to solve situation for Case 3. The relative CFD graphs provide insight into the difference of y measurement corresponding to 60% and 80% of the cumulative distribution for each frequency.

The graph CFD in Fig. 10 is formed by all y measurements values for frequency f. Let Y_j represent the value of Y_{test}-Y_{Max}. If Y_j is less than a, the classification detection accuracy is 80%, while the classification detection accuracy is 60%, for $b < Y_j < a$. The "Not detected" classification referred Y_j greater than b. The summarization of classification for Case 3 is shown Table 6.

The average detection accuracy for position *p2* is referred to average detection accuracy for all frequencies. When the detection accuracy is greater than 60%, the initial code will be

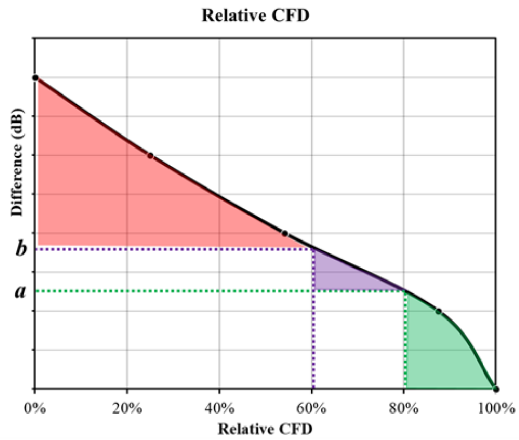

FIGURE 10. Example of CFD graph for frequency, f.

TABLE 6. Threshold value from CFD graph analysis.

Percentage of Detection	Range threshold dB
80%	$Yj < a$
60%	$b < Yj < a$
Not Detected	$Yj > b$

changed from 1 bit to 0 bit. The bit '1' will remain unchanged for the "Not Detected" detection accuracy. The changes of bits from initial code can be seen at output code. The detection efficiency is referred as the percentage of bits change in RF Codes. If all bits of output code are changed, the detection efficiency is 100%, while the detection efficiency is 0% if the bits of output code remain similar to initial code. For example, let say the table of conclusions is for RF Code 111, with positions *p2* and *p6*. The results of *p2* for first bit, second bit, and third bit are 100%, 90%, and 80% Detection, and results of *p6* for first bit, second bit, and third bit are 100%, 90%, and Not Detected, shown in Table 7.

The RF bit code is represented on a detection accuracy percentage scale, with each bit code visualized using circular dots corresponding to different frequencies at specific hidden object positions. A colour scheme is employed to classify detection accuracy, where green and yellow represent Case 1 (100% detection accuracy) and Case 2 (90% detection accuracy), respectively. Blue indicates Case 3 with 80% detection accuracy; brown represents 60% detection accuracy; and red signifies the "Not Detected" case. Fig. 11(a) demonstrates an example of the output Code 111 without any hidden objects, while Fig. 11(b) illustrates the output code from Table 7, where hidden objects

TABLE 7. Threshold value from CFD graph analysis.

Initial Code	Position of hidden object	Percentage of Detection Accuracy (*f1*, *f2*, *f3*)			**Output Code**	**% Detection Efficiency**	**% Average Accuracy Detection**
		Detection at *f1*	Detection at *f2*	Detection at *f3*			
111	*p2*	100	90	80	**000**	**100%**	**90.0**
	p6	100	90	Not detected	**001**	**67%**	**63.3**

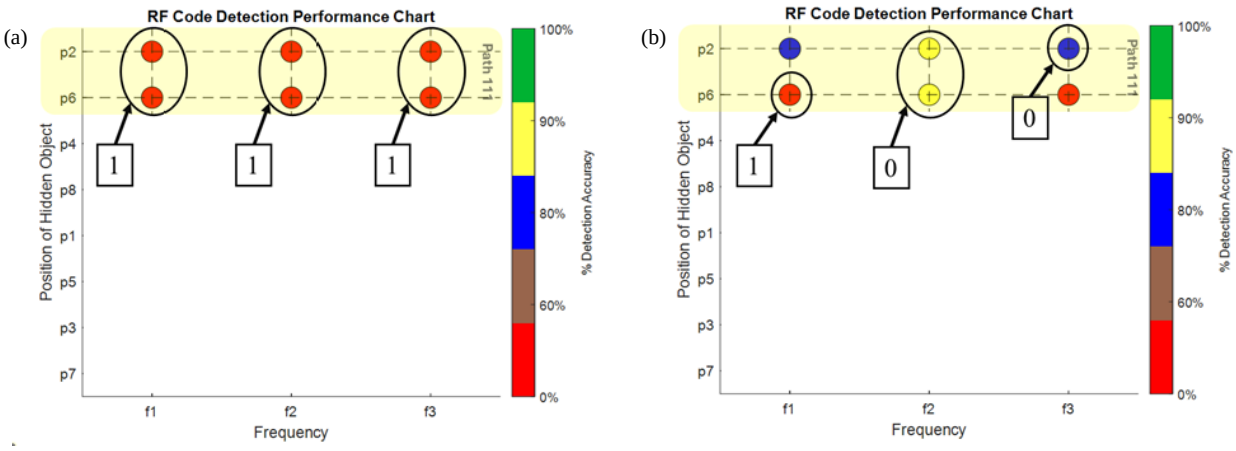

FIGURE 11. Example of RF Code detection performance chart for RF Code 111.

are present. In this example, the green dot at frequency *f1* indicates 100% detection at positions *p2* and *p6*. The yellow dot at frequency *f2*, corresponding to the second bit, reflects 90% detection accuracy. At frequency *f3*, a blue dot signifies 80% detection at position *p2*, while at *p6*, the red dot shows "Not Detected" case.

5. SPATIAL DETECTION ANALYSIS

In this work, Stone has been chosen as Material X and Steel as hidden object for the Spatial Detection measurement. These materials were chosen due to their contrasting electromagnetic properties, particularly in terms of relative permittivity and magnetic permeability. Stone, being a non-metallic material, typically exhibits low permittivity and negligible magnetic permeability, whereas Steel, a conductive and ferromagnetic material, possesses significantly higher values for both parameters. This distinct contrast enhances the interaction with microwave signals, thereby making it suitable for evaluating the effectiveness of the proposed RF Code-based detection system. The measurement process was the same procedure as described in previous section. The measurement result for Y_{test}, Y_{Max}, and Y_{Min} was shown in Table 8 for all positions of hidden object at each frequency. In most positions (*p1*, *p2*, *p5*, *p6*, *p7*, and *p8*), Y_{Max} and Y_{Min} are close to each other, resulting in the narrower Range of Detection. Meanwhile, for positions *p3* and *p4*, Y_{Max} and Y_{Min} have shown a wider gap for each other indicating less reliability. As shown in this figure, for most frequencies, as the frequency increases, there is a significant difference between Y_{Max} and Y_{Min}, indicating that the detection range also increases. The highest difference between Y_{Max} and Y_{Min} can be seen on *f2* for position *p3* which is the value of 5.98 dB. This effect occurs because, at higher frequencies, the wavelength becomes shorter, allowing the signal to interact more effectively with the hidden object. There is only one Y_{test} result in Case 1 that has been found at position *p4* at *f1*. Next, there are four Y_{test} results classified in Case 2, found at frequency *f2* at positions *p2*, *p6*, and *p4*, as well as frequency *f1* at position *p1*. The rest of Y_{test} result is classify as Case 3, indicating lower detection accuracy.

The t-test results for all measured S_{21} data across the tested frequencies and spatial positions showed p-values below 0.05, indicating statistically significant differences between the presence and absence of the hidden object. The CFD graph as shown in Fig. 12 will be used to further classification for Case 3 at *f1*, *f2*, and *f3*. At first, *f1* exhibits the smallest threshold value of 1.25 dB at 80% (a) and 1.89 dB at 60% (b), while the threshold value for *f2* is recorded as 3.45 dB at 80% (a) and 4.40 dB at 60% (b). The highest threshold values of 7.00 dB at 80% (a) and a substantial 12.00 dB at 60% (b) are found at *f3*, which will be used to determine the detection accuracy for the next stage.

Table 9 shows the percentage of detection accuracy across different positions at three frequencies for all path codes. The percentage detection accuracies of 80%, 90%, and 80% are recorded for *f1*, *f2*, and *f3*, respectively for *p2*. The average detection accuracy for path code 111 at position *p2* is 83.3%. The percentage of detection accuracy for position *p6* at *f1* and *f3* has been classified as "Not Detected". While the percentage of detection accuracy of 90% at position p6 was recorded at *f2*. Thus, the average detection accuracy for position *p6* is 30%.

TABLE 8. Figure of Y_{test} with Y_{Max} and Y_{Min} for all positions of hidden object.

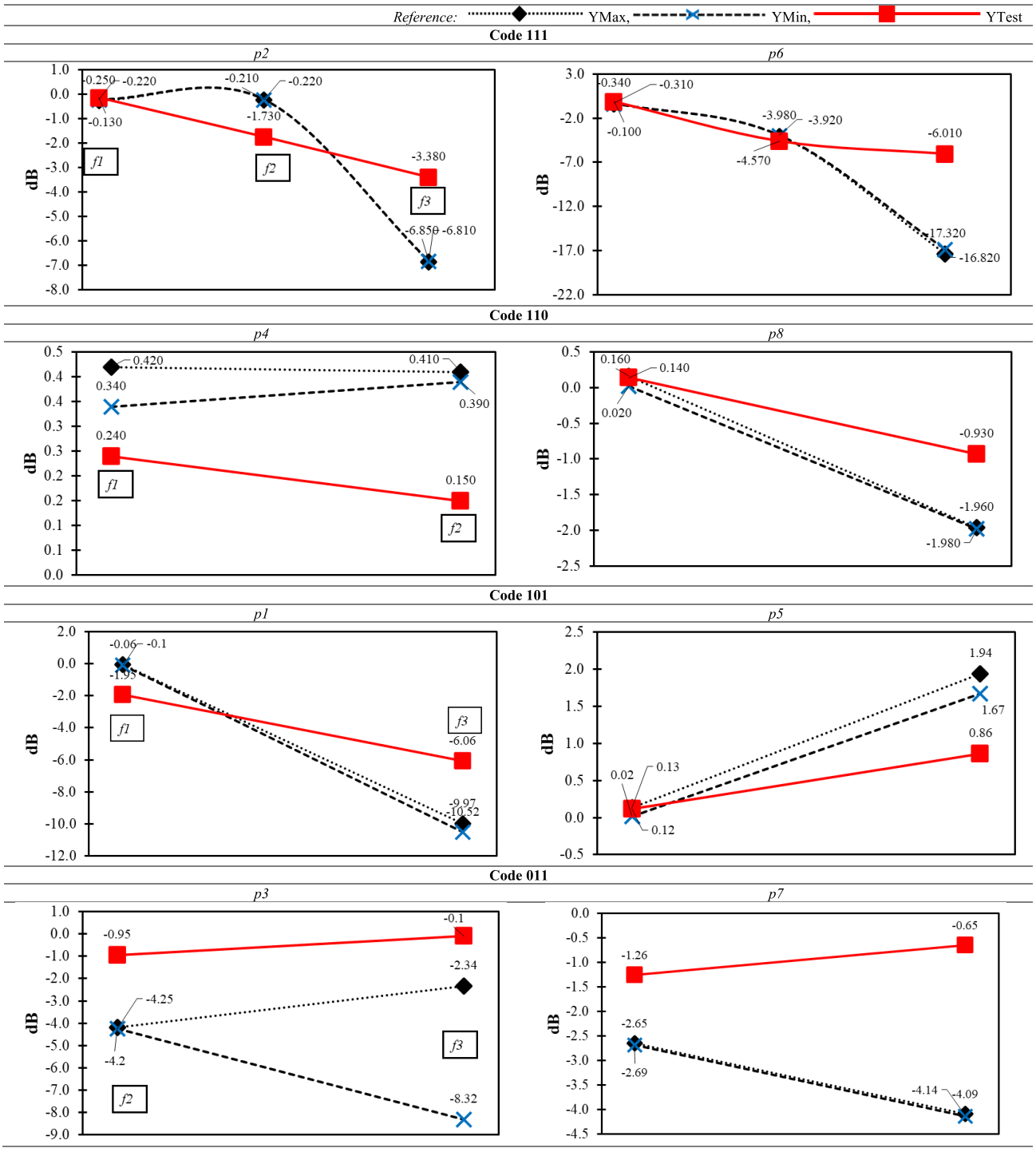

Across all positions, most detection accuracies at *f1* are classified above 80%. However, only position *p6* is classified as Not Detected at *f1*. At *f2*, the detection accuracy exceeds 80%, while at *f3*, it is above 60%. Notably, only position *p6* at *f3* is recorded as Not Detected classification. Moreover, the average detection accuracy for all hidden object positions is recorded more than 70% except position for *p6*. Higher average detection accuracy is recorded for hidden object positions closer to the transmitter sensor. This is maybe due to the higher signal strength that radiates from the transmitter sensor into the hidden object than the position close to the receiver sensor.

Table 10 shows the performance of spatial detection measurement for all RF path codes in terms of detection efficiency and accuracy. The position *p2* for RF path Code 111 recorded detection classification for all three frequencies. Therefore, the initial code of 111 for this position was changed to the output code of bit 000. The changes of all three bits code represent 100% detection efficiency. Conversely, at position *p6*, detec-

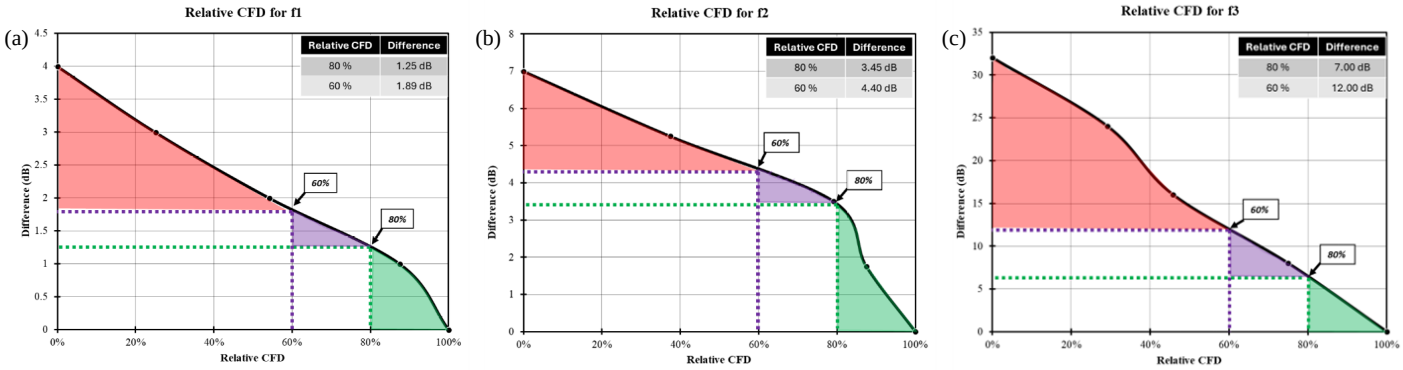

FIGURE 12. Illustrate threshold values for CFD for classification analysis for hidden object (a) *f1*, (b) *f2* and (c) *f3*.

TABLE 9. Percentage of detection accuracy for all RF Codes.

Initial Code	**% Percentage of Detection Accuracy**				**% Average Accuracy Detection**
	Position of hidden object	Detection at *f1*	Detection at *f2*	Detection at *f3*	
111	*p2*	80	90	80	**83.3**
	p6	Not Detected	90	Not detected	**30.0**
110	*p4*	100	90		**95.0**
	p8	80	80		**80.0**
101	*p1*	90		80	**85.0**
	p5	80		80	**80.0**
011	*p3*		80	60	**70.0**
	p7		80	80	**80.0**

TABLE 10. Performance of spatial detection measurement for all RF path codes.

Initial Code	% Percentage of Detection Accuracy				**Output Code**	**% Detection Efficiency**	**% Average Accuracy Detection**
	Position of hidden object	Detection at *f1*	Detection at *f2*	Detection at *f3*			
111	*p2*	80	90	80	**00**	**100**	**83.3**
	p6	Not detected	90	Not detected	**101**	**33**	**30.0**
110	*p4*	100	90		**00**	**100**	**95.0**
	p8	80	80		**00**	**100**	**80.0**
101	*p1*	90		80	**00**	**100**	**85.0**
	p5	80		80	**00**	**100**	**80.0**
011	*p3*		80	60	**00**	**100**	**70.0**
	p7		80	80	**00**	**100**	**80.0**

tion was only registered at *f2*. Therefore, the initial code 111 was changed to output code of 101, while the detection efficiency for *p6* is only 33%. This lower performance at position *p6* is likely due to its proximity to the receiver sensor, where the transmitted signal has already passed through the material and experienced attenuation. As a result, the interaction between the signal and hidden object becomes weaker, making detection less effective than positions near the transmitter, where signal strength is at its peak. For the other positions, the measurement results indicate that the detection classification is recorded across all frequencies. As a result, the initial code was changed to the output code bit 000 for all positions. Thus, the detection efficiency of 100% is registered across all positions. The measurement result analysis shows that the proposed system is able to detect hidden object in all spatial segments except for position *p6*.

Table 11 shows the figures of RF Code detection performance chart that represents the output code at the position of

TABLE 11. RF Code detection performance chart at position (a) *p2*, (b) *p6* and (c) *p4*.

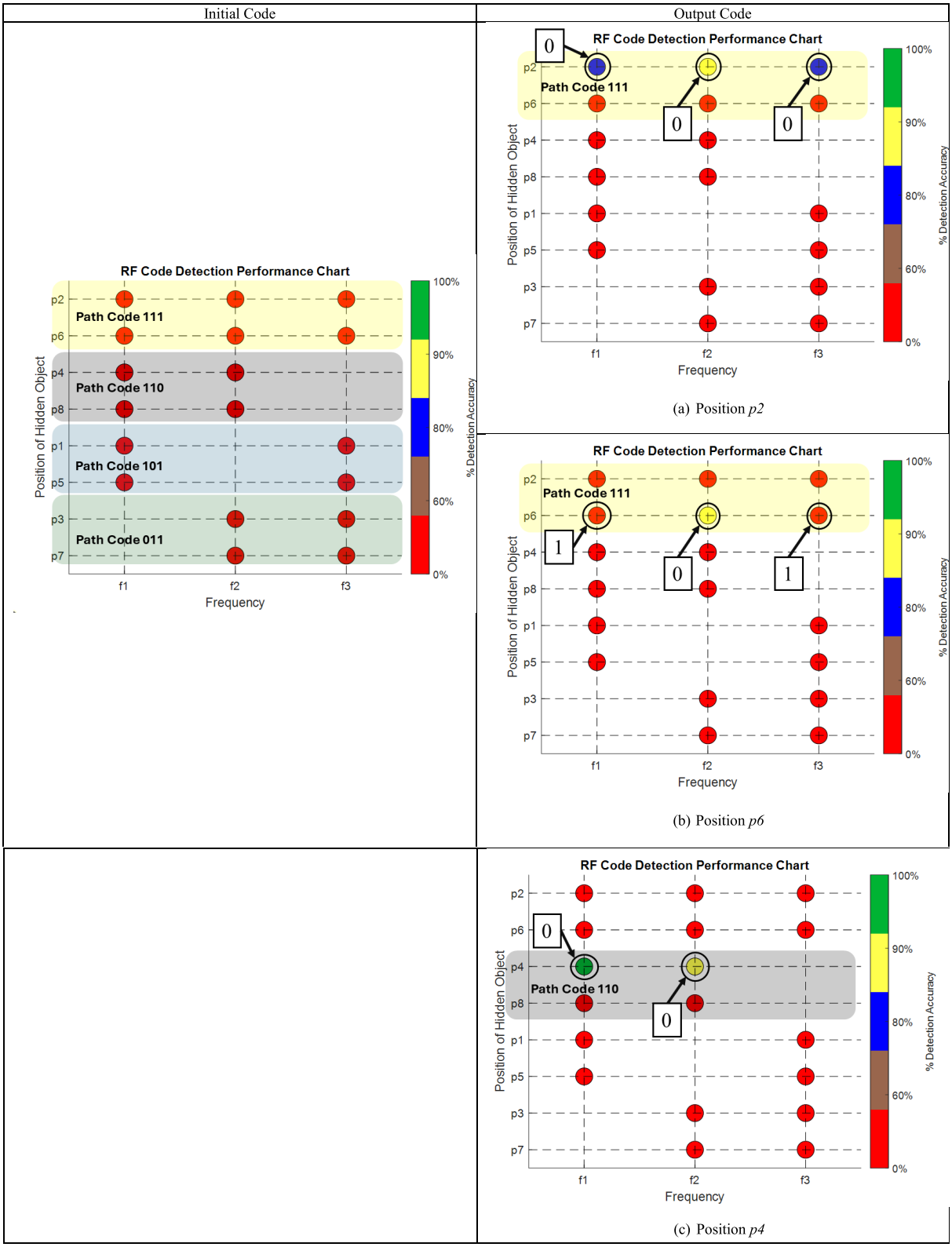

(a) Position *p2*

(b) Position *p6*

(c) Position *p4*

hidden object at *p2*, *p6*, and *p4*. Figures (a), (b), and (c) in Table 11 were constructed based on the percentage of detection accuracy at positions *p2*, *p6*, and *p4* subsequently from Table 10. The blue circular dots (detection accuracy of 80%) were formed at *f1* and *f3* for position *p2* as shown in figure (a), while the yellow circular dot (detection accuracy of 90%) was formed for *f2*. Next, the yellow circular dots was formed at *f2* and red circular dots (detection accuracy of 0%; "Not Detected") appeared at

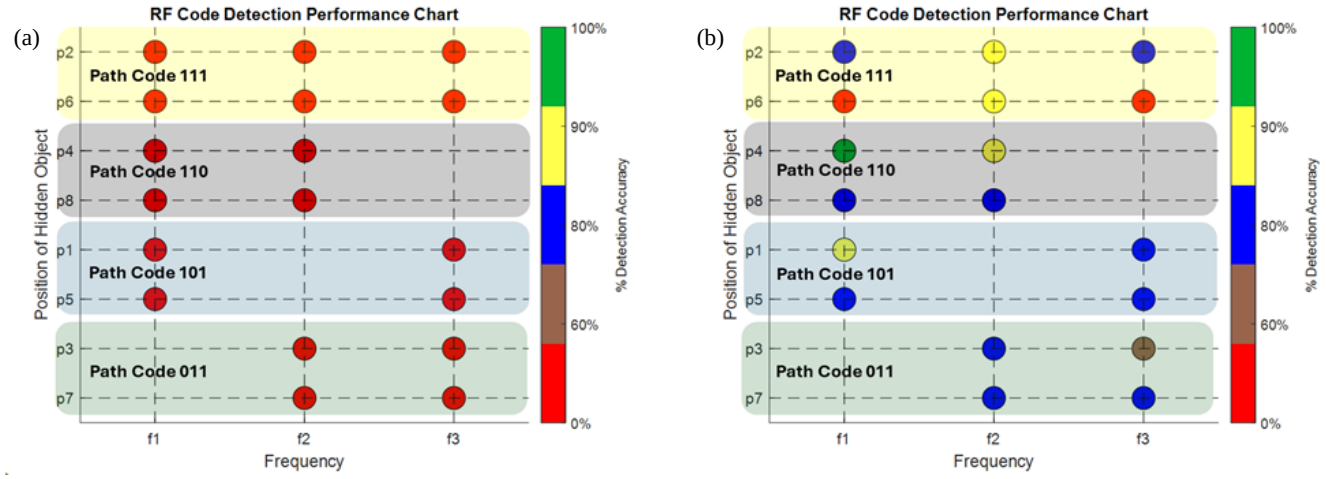

FIGURE 13. Image of RF Code detection performance chart of detection for all codes labelled as: (a) Initial code, (b) output code.

TABLE 12. Comparison of the proposed method with others researcher.

Authors	Detection Focus	Method Used	Image Processing Complexity	Limitations
Tosti *et al.*, [16]	Internal cavity detection in tree trunks (NDT)	GPR (ground-penetrating radar) with microwave tomographic inversion	**High:** Requires full 2D/3D tomographic image reconstruction	Specialized setup (encircling trunk); computationally intensive inversion; effectiveness limited to trunk geometry
Lin, [12]	Medical tumor imaging (early breast cancer detection)	Microwave thermoacoustic tomography (microwave-induced ultrasound imaging)	**High:** Dual-modality imaging (microwave + ultrasound) with complex reconstruction	Complex hardware integration (RF source + acoustic sensors); requires coupling medium; still experimental for clinical use
Tahmid *et al.*, [28]	Object identification via RFID tags (no spatial info)	Chipless RFID tag reading with machine learning classification	**Low:** No image reconstruction (identifies tag code from signal)	Only detects tagged objects (no true localization); requires prior ML training for each tag pattern; not designed for imaging spatial features.
Samsun Zaini *et al.*, [17]	Industrial flow imaging (conductive material distribution)	Electrical Capacitance Tomography (ECT) with segmented electrodes (simulation)	**High:** Tomographic image reconstruction of permittivity distribution	*"Soft-field"* problem – low image resolution and accuracy; requires extensive calibration; study performed in simulation (needs physical validation).
(This work)	Spatial detection of hidden objects (non-destructive)	**RF Code** based microwave sensor array (coded multi-frequency resonators)	**Low:** No complex image reconstruction – interprets coded sensor responses	Tested on limited scenario (one object type and host material); ~70% accuracy in trials

both *f1* and *f3* at position *p6*. The green circular dot (detection accuracy of 100%) was formed at *f1* and yellow circular dots formed at *f2* at position *p4*.

A combined detection accuracy chart for all path codes is presented in Fig. 13 to provide a comprehensive overview of spatial detection performance for the proposed system. It is important to note that the combined image does not represent simultaneous path code measurements. Rather, it is a compilation of separately conducted experiments, with each path code measured independently to ensure accurate analysis and comparison. It is noted that the different colours of circular dots can be found for all positions. It shows that the system is able to perform spatial detection with the minimum efficiency of 33%. One green circular dot (detection accuracy of 100%) and one brown circular dot (detection accuracy of 60%) are found at positions *p4* and *p3*, respectively. There are only two red circular dots (Not Detected) found at *p6* at frequencies *f1* and *f3*. The system successfully detected the hidden object at frequency *f2* across all positions. As a result, no red circular dots were observed at *f2*, indicating consistent detection. Table 12 presents

related research works that have been conducted in the field of object detection, focusing on aspects such as detection focus, method used, image processing complexity, and limitations.

6. CONCLUSION

The proposed Microwave-Based Object Localization System for spatial detection using RF Code technique was successfully presented. The performance analysis has been done to evaluate the percentage detection accuracy throughout the positions of hidden objects and frequencies of the RF Code. The detection performance of this system with 70% average detection accuracy was registered for most of the positions. The detection efficiency recorded 100% detection efficiency for most of the RF path codes. The proposed RF Code performance chart shows the effectiveness of the proposed system in spatial detection measurements without using any complex algorithms. These findings indicate that RF Code technique has significant potential for applications in nondestructive testing and material analysis, offering enhanced detection capabilities for various industrial and research scenarios. In future developments, the system may be further improved by integrating machine learning algorithms to automatically classify patterns in the S_{21} signal loss data and enhance detection precision. Moreover, the application of this technique could be broadened by testing it on a wider range of materials with different dielectric properties — such as wood, plastic, or composites — to explore its adaptability across various industrial conditions. Such improvements could increase the robustness and scalability of the RF Code-based spatial detection system, making it suitable for more complex or dynamic sensing environments. Furthermore, the study offers theoretical implications by demonstrating that frequency-coded resonance can be used to infer the spatial presence of hidden objects, eliminating the need for complex image reconstruction. The system also provides practical benefits through its low-complexity implementation, which is suitable for real-time or embedded applications. Nonetheless, this study acknowledges limitations, particularly in the diversity of tested materials and controlled experimental setup. Future work will aim to address these limitations by incorporating real-time embedded system integration, extending the detection framework for multiple hidden objects, and employing machine learning models to improve pattern analysis and detection accuracy.

ACKNOWLEDGEMENT

This work was supported by the Universiti Teknikal Malaysia Melaka under the FRGS research grant (FRGS/1/2021/FKEKK/F00471), and by the Ministry of Higher Education of Malaysia.

REFERENCES

[1] Origlia, C., D. O. Rodriguez-Duarte, J. A. T. Vasquez, J.-C. Bolomey, and F. Vipiana, "Review of microwave near-field sensing and imaging devices in medical applications," *Sensors*, Vol. 24, No. 14, 4515, Jul. 2024.

[2] Sobkiewicz, P., P. Bieńkowski, and W. Błażejewski, "Microwave non-destructive testing for delamination detection in layered composite pipelines," *Sensors*, Vol. 21, No. 12, 4168, Jun. 2021.

[3] Tao, Y. H., A. J. Fitzgerald, and V. P. Wallace, "Non-contact, non-destructive testing in various industrial sectors with terahertz technology," *Sensors*, Vol. 20, No. 3, 712, 2020.

[4] Liu, C., C. Wang, W. Zhang, R. Martinez-Lopez, and J. Martinez-Lorenzo, "Microwave-induced thermoacoustic imaging of subsurface 3D water-oil displacement in porous sand," *Authorea Preprints*, Jul. 2024.

[5] Hampel, U., L. Babout, R. Banasiak, E. Schleicher, M. Soleimani, T. Wondrak, M. Vauhkonen, T. Lähivaara, C. Tan, B. Hoyle, and A. Penn, "A review on fast tomographic imaging techniques and their potential application in industrial process control," *Sensors*, Vol. 22, No. 6, 2309, Mar. 2022.

[6] Ranieri, G., S. V. Calcina, and L. Piroddi, "Preventive geophysical surveys for the evaluation of the archaeological risk: Examples from the region of the ancient Pylos (western Peloponnese, Greece)," in *2021 21st International Conference on Computational Science and Its Applications (ICCSA)*, 242–250, Cagliari, Italy, Sep. 2021.

[7] El Masri, Y. and T. Rakha, "A scoping review of non-destructive testing (NDT) techniques in building performance diagnostic inspections," *Construction and Building Materials*, Vol. 265, 120542, Dec. 2020.

[8] Och, A., P. A. Hölzl, S. Schuster, S. Scheiblhofer, D. Zankl, V. Pathuri-Bhuvana, and R. Weigel, "High-resolution millimeter-wave tomography system for nondestructive testing of low-permittivity materials," *IEEE Transactions on Microwave Theory and Techniques*, Vol. 69, No. 1, 1105–1113, Jan. 2021.

[9] Aldhaeebi, M. A., K. Alzoubi, T. S. Almoneef, S. M. Bamatraf, H. Attia, and O. M. Ramahi, "Review of microwaves techniques for breast cancer detection," *Sensors*, Vol. 20, No. 8, 2390, Apr. 2020.

[10] Ruvio, G., R. Solimene, A. Cuccaro, G. Fiaschetti, A. J. Fagan, S. Cournane, J. Cooke, M. J. Ammann, J. Tobon, and J. E. Browne, "Multimodal breast phantoms for microwave, ultrasound, mammography, magnetic resonance and computed tomography imaging," *Sensors*, Vol. 20, No. 8, 2400, Apr. 2020.

[11] Islam, M. T., M. T. Islam, M. Samsuzzaman, S. Kibria, and M. E. H. Chowdhury, "Microwave breast imaging using compressed sensing approach of iteratively corrected delay multiply and sum beamforming," *Diagnostics*, Vol. 11, No. 3, 470, Mar. 2021.

[12] Lin, J. C., "Microwave thermoacoustic tomographic (MTT) imaging," *Phys. Med. Biol.*, Vol. 66, No. 10, 10TR02, May 2021.

[13] Benny, R., T. A. Anjit, and P. Mythili, "An overview of microwave imaging for breast tumor detection," *Progress In Electromagnetics Research B*, Vol. 87, 61–91, 2020.

[14] AlSawaftah, N., S. El-Abed, S. Dhou, and A. Zakaria, "Microwave imaging for early breast cancer detection: Current state, challenges, and future directions," *Journal of Imaging*, Vol. 8, No. 5, 123, 2022.

[15] Shao, W. and T. McCollough, "Advances in microwave near-field imaging: Prototypes, systems, and applications," *IEEE Microwave Magazine*, Vol. 21, No. 5, 94–119, May 2020.

[16] Tosti, F., G. Gennarelli, L. Lantini, I. Catapano, F. Soldovieri, I. Giannakis, and A. M. Alani, "The use of GPR and microwave tomography for the assessment of the internal structure of hollow trees," *IEEE Transactions on Geoscience and Remote Sensing*, Vol. 60, 1–14, 2021.

[17] Samsun Zaini, N. A. H., H. Wahid, R. A. Rahim, J. Jamaludin, M. F. Ramli, N. Ahmad, A. A. Hamzah, and F. A. J. Mohamad,

"A simulation of single and segmented excitation in electrical capacitance tomography system," in *Methods and Applications for Modeling and Simulation of Complex Systems*, 171–179, 2023.

[18] Shao, W. and Y. Du, "Microwave imaging by deep learning network: Feasibility and training method," *IEEE Transactions on Antennas and Propagation*, Vol. 68, No. 7, 5626–5635, Jul. 2020.

[19] Feng, C., W. Zhang, L. Li, L. Han, X. Chen, and R. Ma, "Angle-based chipless RFID tag with high capacity and insensitivity to polarization," *IEEE Transactions on Antennas and Propagation*, Vol. 63, No. 4, 1789–1797, Apr. 2015.

[20] Khan, M. M., F. A. Tahir, M. F. Farooqui, A. Shamim, and H. M. Cheema, "3.56-bits/cm^2 compact inkjet printed and application specific chipless RFID tag," *IEEE Antennas and Wireless Propagation Letters*, Vol. 15, 1109–1112, 2015.

[21] Kim, S., A. Georgiadis, and M. M. Tentzeris, "Design of inkjet-printed RFID-based sensor on paper: Single- and dual-tag sensor topologies," *Sensors*, Vol. 18, No. 6, 1958, Jun. 2018.

[22] Miao, F., J. Dai, B. Tao, M. Zhao, and P. K. Chu, "Multifrequency-coded RFID microstrip photosensor based on ZnOAgCuS nanocomposites," *IEEE Transactions on Electron Devices*, Vol. 71, No. 11, 7002–7009, 2024.

[23] Le, C.-C., T.-K. Dao, N.-Y. Pham, and T.-H. Nguyen, "Inverted frequency-coded chipless RFID tag design methodology based on parameter optimization," *IEEE Microwave and Wireless Technology Letters*, Vol. 34, No. 12, 1399–1402, 2024.

[24] Zhang, R., S. Wang, H. Liu, H. Huang, J. Yu, and Y. Guan, "When noise can help: Anonymous group writing in RFID-enabled backscatter networks," *IEEE Transactions on Mobile Computing*, Vol. 23, No. 12, 13 760–13 772, 2024.

[25] Bala Subramanian, C., P. Nagaraj, P. M. S. Rao, P. Sukrutha, D. L. Poojitha, and S. G. Ram, "Implementing an effortless shopping experience: Smart trolley and billing system using IoT," in *2024 5th International Conference on Electronics and Sustainable Communication Systems (ICESC)*, 291–299, Coimbatore, India, Aug. 2024.

[26] Chen, Z., Y. Yang, X. He, and S. Xiao, "A RFID chipless tag based on hybrid frequency-polarization coding," in *2024 IEEE 7th International Conference on Electronic Information and Communication Technology (ICEICT)*, 296–301, Xi'an, China, 2024.

[27] Chien, H.-Y., *The Study of RFID Authentication Protocols and Security of Some Popular RFID Tags*, INTECH Open Access Publisher, 2009.

[28] Pranto, T. H., M. N. Neloy, A. A. Noman, S. Wasif, M. A. Wahab, and R. M. Rahman, "Utilizing deep learning in chipless RFID tag detection: An investigation on high-precision mm-Wave spatial tag estimation from 2D virtual imaging," *Journal of Information and Telecommunication*, Vol. 8, No. 3, 361–383, 2024.

[29] Mulloni, V. and M. Donelli, "Chipless RFID sensors for the internet of things: Challenges and opportunities," *Sensors*, Vol. 20, No. 7, 2135, Apr. 2020.

[30] Kiani, S. H., H. S. Savci, M. E. Munir, A. Sedik, and H. Mostafa, "An ultra-wide band MIMO antenna system with enhanced isolation for microwave imaging applications," *Micromachines*, Vol. 14, No. 9, 1732, Sep. 2023.